Theoretical Investigations and Comparisons of the Amorphous Structures of Adamantane-like Cluster Materials Utilizing Molecular Dynamics Simulations

Sebastian Schwan, Benjamin D. Klee, Niklas Rinn, Peter R. Schreiner, Stefanie Dehnen, Wolf-Christian Pilgrim, and Doreen Mollenhauer*

ABSTRACT: Cluster materials of the composition AdR_4 (Ad = adamantane, R = organic substituent) and $[(RT)_4E_6]$ (R = organic substituent; T = Si, Ge, Sn; and E = S, Se, Te) exhibit directional white light emission or produce second harmonics when irradiated with a continuous wave infrared laser source. The nature of the nonlinear optical properties correlates with the macroscopic structures of the cluster materials. The desired white light emission predominantly occurs in amorphous materials. It is therefore crucial to understand the geometric structures of the materials and the order within the materials. Here, we investigate the geometric structures of 12 different a damantane-like c luster m aterials by molecular dynamics simulations using a nonperiodic particle approach. The comparison of the calculated structure factors for two cluster materials with the corresponding experimental data obtained from diffraction and EXAFS measurements shows very good agreement. Our computations revealed that, on the one hand, larger, more flexible core structures (Ad < $\{Si_4S_6\}$ < $\{Ge_4S_6\}$ < $\{Sn_4S_6\}$) tend to lead to amorphous solids. On the other hand, larger substituents (methyl < phenyl < naphthyl) lead to more defined nearest neighbor interactions, with a tendency toward crystalline solids. Overall, our results show that a beginning order in the material results from a combination of the degree of flexibility of the core structure and the variation of the nearest neighbor interaction determined by the substituents.

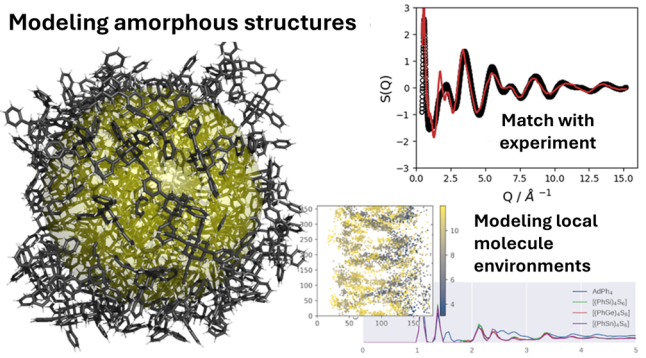

INTRODUCTION

Recent discoveries of tetrel chalcogenide cluster materials show that their nonlinear optical behavior enables the highly directional emission of a continuous white light spectrum upon excitation with a continuous infrared light source.[1,2] A comparable effect can only be achieved by intense, short, pulsed laser sources, which limits the applicability to specific tasks in medicine and science.[3−8] The molecular tetrel chalcogenide cluster materials discussed here have unique structures with an adamantane-like core 1,3,5,7-tetrasubstituted with organic substituents. The composition of the organic materials is AdR_4 (Ad = adamantane, R = organic substituent)[9,10] and the composition of the inorganic materials is $[(RT)_4E_6]$ (R = organic substituent, T = Si, Ge, Sn and E = S, Se, Te).[1,11−14] Exemplary structures of the individual clusters are shown in Figure 1.

The materials with different combinations of cores and substituents investigated here experimentally give solid state structures with crystalline or amorphous habitus. Structures with amorphous habitus have some short-range order, but lack the long-range order that is present in crystalline materials.[15] Experimental studies have shown that these materials exhibit

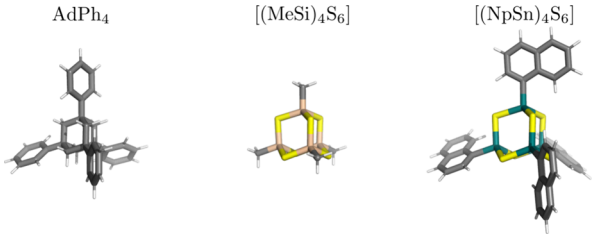

Figure 1. Minimum monomer structures optimized at the B3LYP-D3(BJ)/cc-pVDZ level of theory. Left: $AdPh_4$; middle: $[(MeSi)_4S_6]$; right: $[(NpSn)_4S_6]$. Color code: gray: carbon; white: hydrogen; yellow: sulfur; brown: silicon; green: tin.

directional white light generation (WLG) whereas second harmonic generation (SHG) occurs when they are crystalline.[1,11,14] This correlation between optical and structural properties raises the question of why certain combinations of adamantane-cores and substituents lead to amorphous or crystalline materials.

This question has already partially been addressed by experimental and computational studies.[11,16] The systematic analysis of 12 cluster materials, modeled with a dimer system in which two monomers interact with each other, provided insights into the fundamental interactions of the molecules in the material.[16] The 12 compounds show increasing core radii and different substituent symmetry, size and flexibility, in particular AdR_4 (Ad = adamantane) and $[(RT)_4S_6]$ (T = Si, Ge, Sn) with R = methyl, phenyl, or 1-naphthyl were considered. Decomposition of the binding energy within the cluster dimers allows to distinguish between materials dominated by substituent-substituent interactions and those dominated by core−core interactions. While the isotropic core−core interaction can be associated with a lower tendency for order in the materials, a higher degree of order can be expected for the dominant substituent-substituent interactions. Thus, the decomposition of the cluster dimer interactions can serve as a rough indicator for the order in the material. This approach was already successful in comparing $[(Np/PhSn)_4S_6]$ and $\{Si_4S_6\}$-based homologues and agrees with the experimental studies.[11]

Another recent study indicates that $[(NpSn)_4]S_6$ has bulk amorphous and crystalline regions, which is also consistent with almost 50% core−core and 50% substituent-substituent interactions in the dimer model.[17] These results show that the onset of order, probably due to π-stacking, is sufficient to increase long-range order and crystallinity. At the same time, the equally strong core−core interactions lead to overall amorphous materials. However, the dimer model cannot estimate the macroscopic structure of materials for which the difference between the core−core and the substituent-substituent interaction is small, such as crystalline $[(PhSi)_4S_6]$ and amorphous $[(PhGe)_4S_6]$. Furthermore, an extension of the dimer model to trimer and tetramer model systems revealed similar trends in the binding energies compared to the dimer model, but also showed the need for larger model systems to describe the geometric structures.[16]

In this study, we aim to uncover further structural differences between the same 12 compounds by modeling their geometric structurex considering larger aggregates. The modeling of amorphous materials is computationally challenging because periodic boundary conditions lead to translational symmetry and thus long-range order in the system. Periodic systems that are large enough to overcome these constraints are hardly computationally accessible.[15] Therefore, instead of calculating large periodic supercells, we use a particle approach to analyze a nonperiodic model system and to eliminate translation symmetry. To be able to perform the computations of large particle systems of organic and inorganic adamantane-based cluster materials, we used the GFN-FF force field.[18] In total, we performed molecular dynamics (MD) simulations of particles containing 100 molecules of the 12 different compounds. Thus, particles with a diameter of about 0.4 to 0.6 nm were simulated without periodic boundary conditions.

We aim to investigate the influence of the chemical composition on the near and beginning order and geometric structure within large amorphous particles. Therefore, we analyzed the particles in detail. We gained first fundamental insight into the geometric composition and the binding parameters by analyzing the density and the distribution of bond lengths and angles. Furthermore, more detailed insight into the coordination of the molecular and atomic distribution within the amorphous materials were obtained by analyzing pair distribution functions (PDF), angle-dependent neighborhood plots, and results from a similarity analysis.

COMPUTATIONAL DETAILS

The geometric structures for each molecular clusters were located using a conformer search algorithm followed by optimization. For the conformer search, the iterative metadynamics with the genetic structure crossing (iMTD-GC) algorithm[19,20] was used, followed by optimization steps at the GFN2-xTB level of theory. The GFN2-xTB method is implemented in the xTB software package version 6.4.1.[21−23,24] The optimized monomer structures of all compounds are shown in Figure S1.

For method evaluation, we compared the cluster dimer structures from our previous study[16] with cluster dimers optimized with the GFN-2-xTB and GFN-FF methods (SI, Figure S2). We found that the GFN2 and GFN-FF methods generally reproduce the DFT-optimized structures quite well (average RMSD compared to the B3LYP-optimized structure: 0.11 Å for GFN2 and 0.33 Å for GFN-FF). Only for structures with large substituents the deviations from DFT-optimized structures are somewhat larger due to rotations of the substituents (see Figure S3 for an example). The core−core distances are similar for all systems tested and, in some cases, GFN-FF performed better than GFN2-xTB. This suggests that GFN-FF represents a reasonable choice for the simulation of extended particles.

For the initialization of the amorphous particles, Packmol was used to generate a square box with a random distribution of 100 molecules and a density of 0.5 g/cm^3.[27] These large particles were optimized and used as initial structures for the molecular dynamics simulations at the GFN-FF level of theory.[18] All GFN2-xTB (monomer structures) and GFN-FF (particles of 100 molecules) computations were performed without periodic boundary conditions. The large particles of the different compounds were preoptimized with the GFN-FF and then MD simulations were performed at 300 K for 100 ps with a time step of 1 fs at the same level of theory. We used a hydrogen mass of 4, as this prevents unphysical vibrations of the hydrogen atoms and improves the stability of the MD simulations.[22]

From each MD simulation, the structure was exported every 1 ps. This results in 100 exported frames that are not too alike to each other due to their 1 ps difference. Only the last 50 frames were used for the analysis, because the particles need some time to reach the equilibrium density. In experimental studies, these materials do not form small particles but solids, and in some cases even glasses.[1,9,11,14,25,26] So the internal molecules in the bulk dominate the properties of the materials and the surface molecules have only a small effect. To account for this phenomenon, we removed the surface molecules of the particles after the simulation, leaving only molecules representing the bulk material of an amorphous solid.

For the validation of the particle approach, the structure factors S(Q) was compared to the experimentally observed structure factors. The RMC_POT software[27] was used to calculate S(Q) and χ(k) for $[(PhSn)_4S_6]$ and $[(NpSn)_4S_6]$ in

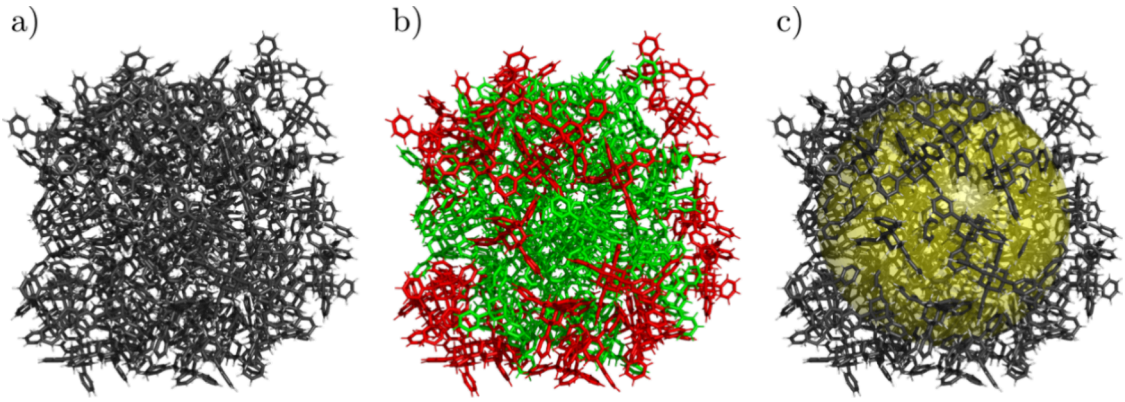

Figure 2. Particles of 100 $AdPh_4$ molecules obtained from MD simulations. (a) Complete particle as obtained from the MD simulation, (b) green: bulk molecules, red: surface molecules, which are neglected for the following analysis, (c) complete particle inside a sphere, which is used to calculate the density of the material.

order to compare the simulation results with experimental data. This calculation is done based on the atomic coordinates of the considered molecules (later on called bulk molecules) assuming that they form a particle surrounded by vacuum. To increase statistics and avoid Fourier-transformation artifacts due to the limited size of the model S(Q) and χ(k) for the last five frames of the MD simulation were averaged. The model being nonperiodic means that the calculated S(Q) is not quantitatively comparable to data measured on bulk samples especially for the lower Q region.

Methods Used for Analysis. The calculated MDs were processed and analyzed in different ways. Since we want to analyze the bulk properties of the materials, the result of the MD simulations obtained with the particle approach was processed in steps I and II.

I) Based on the geometric structure of each frame [see Figure 2a)], we detected each molecule and calculated its center of mass. From the distribution of molecular centers, we used the python package scipy[28] to calculate the convex hull. The convex hull method creates a unique, convex polygon whose vertices are the outermost centers of mass of the molecules within the particle and which contains all the points of the particle. The molecules whose points define the convex polygon are referred to as surface molecules, and the molecules within the polygon are referred to as bulk molecules [Figure 2 b)]. We separated the surface molecules from the bulk molecules for further analysis, leaving about 50−70 molecules that are bulk molecules.

II) After defining the molecules of the bulk, the density of the material was determined. As we have chosen a particle approach for the simulations, it is not possible to simply divide the total atomic mass of the system by the cell size. Instead, a spherical volume was defined with its center at the center of mass of the whole system. The radius of this sphere is defined as the distance between the center of the whole system and the center of mass of the molecule of the defined bulk region of the particle, which has the greatest distance from the center. This results in a sphere inside the particle as shown in Figure 2 c). The sum of all the masses of all the atoms within this defined sphere was used to determine the total mass within the given volume of the sphere. The density was then calculated as the quotient of this mass and the volume of the sphere.

For the identified bulk molecules, the structural parameters were determined by calculating all bond lengths and angles of the selected 50 frames (after 50 ps of the trajectory). A histogram was generated from the extracted bond lengths and angles. Based on this histogram, a Gaussian function (equation 1) was fitted to the data to provide insights into the average bond lengths and angles (x) and their standard deviation.

$$f(x) = \frac{e^{-x'/2}}{\sqrt{2\pi}} \tag{1}$$

The total pair distribution function (PDF) of the defined bulk of the particle was also calculated using equation 2. The value of the PDF is related to g(r), where r is the radius around each point in equation 2).

$$g(r) = \sum_{i}^{N} \sum_{j \neq i}^{N} \delta(r - r_{ij}) \tag{2}$$

Various PDFs were calculated, which are powerful tools for examining specific distances within the given structure. It allows us to identify patterns within the structure of the particles and locate differences in peak location, height, and width, all of which correlate with the overall structure. We generated three different PDFs by considering i) all atoms, except hydrogen, ii) the center of mass of the molecules, and iii) the center of mass of the substituents. However, only the dependence on radius is considered in the PDFs.

To account for the angular dependence of the relative orientation of the molecules, all possible molecule dimers were extracted from the trajectory. We defined a coordinate system relative to one of the molecules in the dimer, the reference molecule. The origin of the coordinate system is the center of mass of the reference molecule. The three axes are orientated at 90° to each other. The x-axis is aligned along one substituent. The second is at 90° to the first one, so that the x-y plane is oriented directly in the direction of the second substituent. The orientation of the third axis follows from the first two axes and is oriented perpendicular to the paper plane (Figure 3).

This provides insights into the angular distribution of the molecules within the particle. The position of the second molecule of the dimer is defined and plotted by determining the tilt of the center of mass of the molecules relative to the x-axis (polar angle θ) and the y-axis (azimuth-angle φ) (Figure 3). For a more complete picture, we additionally determined the core−core distances of the centers of mass of the molecular core structures within the dimers. These core−core distances

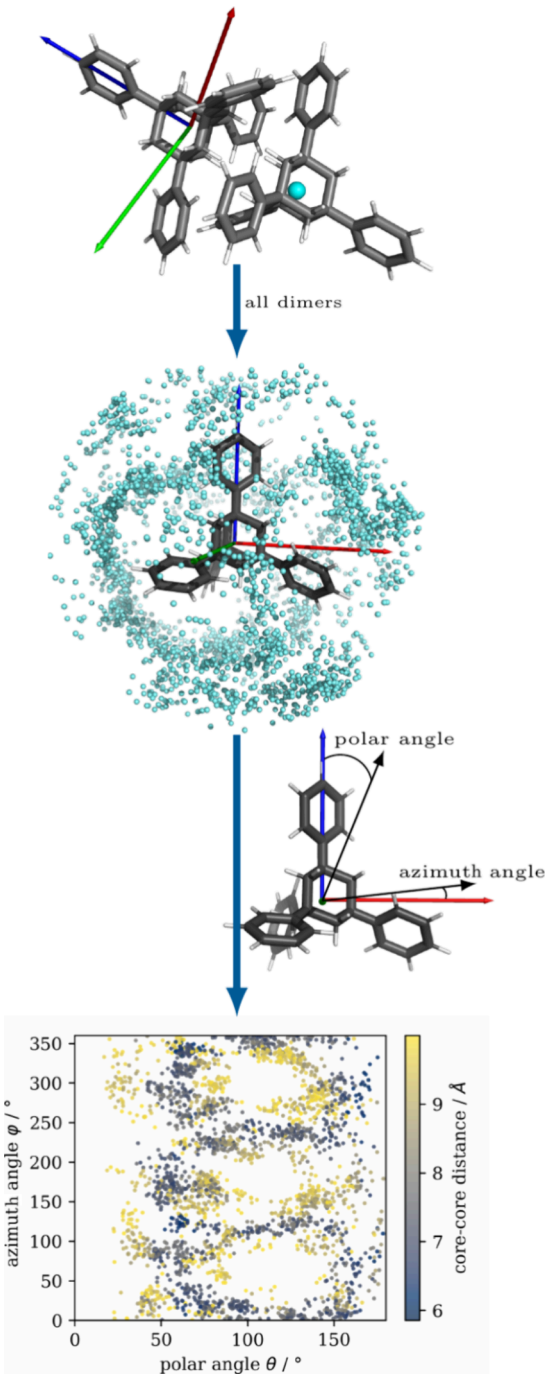

Figure 3. Demonstration of the orientation of two molecules relative to each other for the angle-dependency analysis demonstrated on the example $AdPh_4$. Gray: carbon, white: hydrogen, blue: mass center of other molecules.

of the dimers are represented by a range of colors in Figure 3. The total number of dimers greatly varies depending on the chemical composition of the molecular material, ranging from 7725 extracted dimers for $[(NpSn)_4S_6]$ to 20671 extracted dimers for $[(MeGe)_4S_6]$. As a cutoff for the core−core distance, we chose two times the equilibrium core−core distance of the minimum dimer. These core−core distances of the energetically preferred dimers are 6.16 Å for $AdMe_4$, 6.21 Å for $[(MeSi)_4S_6]$, 6.24 Å for $[(MeGe)_4S_6]$, 6.18 Å for $[(MeSn)_4S_6]$, 5.89 Å for $AdPh_4$, 6.02 Å for $[(PhSi)_4S_6]$, 6.07 Å for $[(PhGe)_4S_6]$, 6.17 Å for $[(PhSn)_4S_6]$, 5.97 Å for $AdNp_4$, 6.19 Å for $[(NpSi)_4S_6]$, 6.43 Å for $[(NpGe)_4S_6]$, and 6.80 Å for $[(NpSn)_4S_6]$ computed at the DFT level of theory.[16]

Finally, we analyzed the extracted dimer structures for structural similarity. Therefore, the smooth overlap of atomic potential (SOAP) method implemented in the Python module *dscribe* was used to generate a power spectrum, which is a very large vector with no physical meaning for each dimer structure.[29−32] Because different chemical compounds contain different elements, the SOAP package defines different atomic potentials for them. This means that dimer structures with different elements cannot be compared. To avoid this and to make the different chemical compositions comparable, we used the same core potentials for all heavy atom types (C, S, Si, Ge, Sn). The hydrogen atoms have been removed for this analysis.

The obtained power spectra are highly dimensional and therefore not suitable for presentation in two dimensions. Therefore, the dimensionality of the power spectra was reduced to a 2D scatter plot using the Principle Component Analysis (PCA) implemented in the scikit-learn Python module.[28] The 2D scatter plots allow a simple comparison of the purely geometric features of the extracted dimer structures. We compared the 2D scatter plots of the structures with the same composition (core structure and substituents), which has already proved useful in studies of the configurational space of various organic molecules,[30] the solid structure of azaphenacenes,[33] the formation of various ice-structures,[34] and the solid-state structures of phenacenes.[35]

Comparison with Experimental Data. Figure 4 shows the experimentally obtained S(Q) and χ(k) in comparison to those calculated by RMC_POT.[36,37] For both $[(PhSn)_4S_6]$ and $[(NpSn)_4S_6]$ the calculated data are in general good agreement with the experimental data. However, for S(Q) slight shifts in peak positions are visible and the double peak structure at Q ≈ 11 Å is not reproduced by the MD simulation. This indicates that the interatomic distances in the intramolecular structure differ only slightly for both samples. A similar observation can be made regarding the EXAFS data, where signal shifts are visible. Since Sn is the absorbing species for the EXAFS data, and Sn and S are the main contributors to the X-ray scattering, the data suggest that these shifts are caused by small errors in the Sn−S bonds. Since significant molecular distortions have been found for $[(PhSn)_4S_6]$ but not for $[(NpSn)_4S_6]$, the observed shifts are unlikely to be related to significant molecular distortions.[38] Considering these findings, we conclude that the MD simulation results are sufficiently supported by experimental data and assume that this applies to all other materials presented in this study for which experimental data are not available. The assumption of transferability is further supported by the fact that the GFN-FF force field showed a larger RMSD for monomers and dimers of the cluster materials with Sn than for purely organic compounds or compounds with Si or Ge (see SI, Figure S2).

RESULTS

Densities. First, the density of the bulk of the particles was analyzed. The densities and the average atomic weights of the different material compositions of the particles are shown in Figure 5 and Table S1. Experimental density values are only available for seven compounds in their crystalline structure: $[(MeT)_4S_6]$ (T = Si, Ge, Sn), $AdPh_4$, $[(PhSi)_4S_6]$, $[(PhSn)_4S_6]$, and $[(NpSn)_4S_6]$. The particle approach delivers a density very close to the experimentally observed density of crystalline $AdPh_4$ (determined: 1.260 g cm^{-3}, experimentally

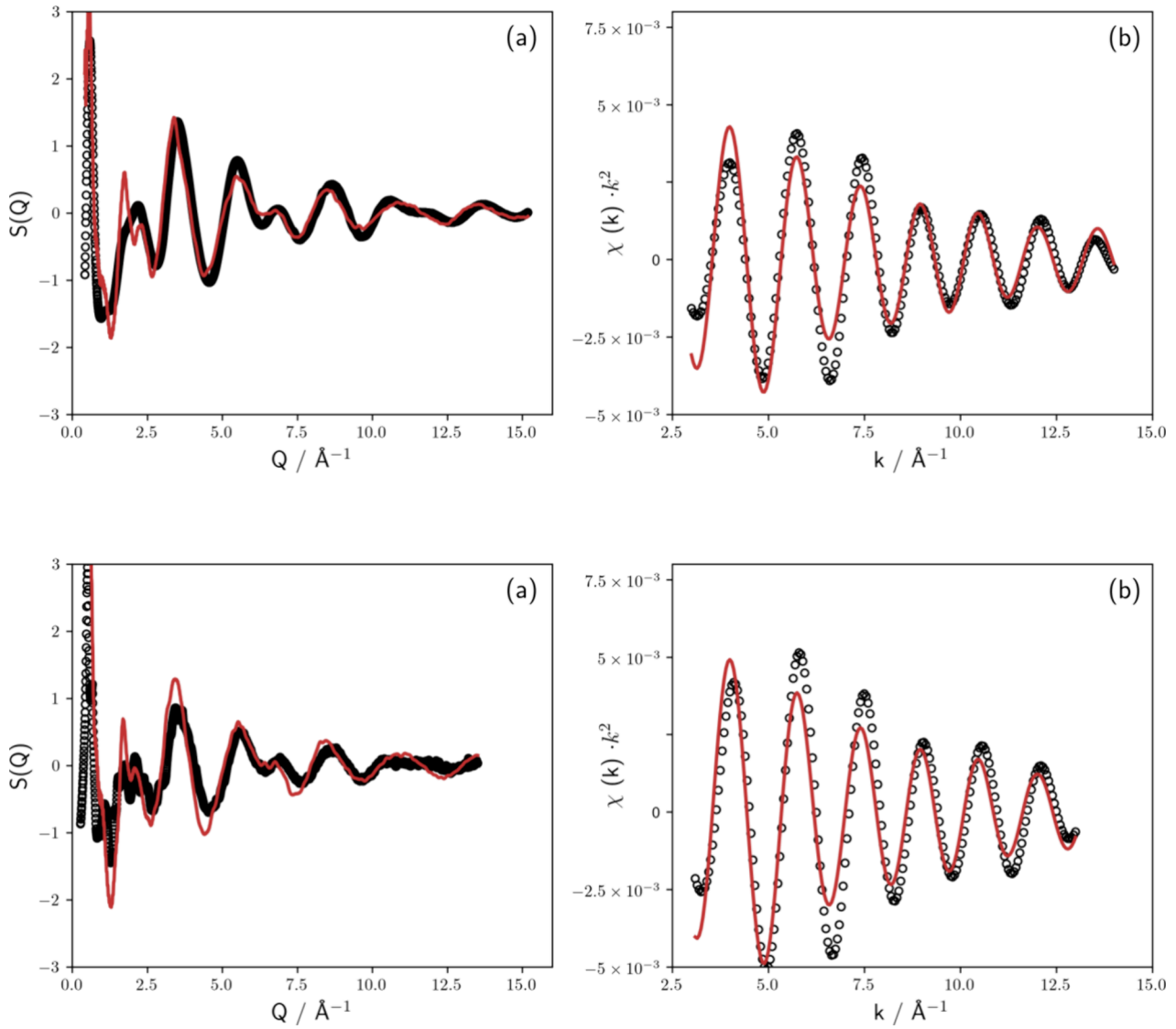

Figure 4. Experimental (black circles) and calculated (red line) S(Q) (a) and χ(k) (b) are shown for $[(PhSn)_4S_6]$ (top) and $[(NpSn)_4S_6]$ (bottom).

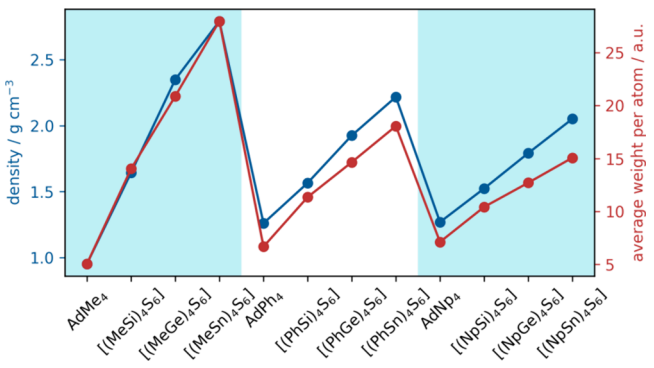

Figure 5. Calculated densities (blue) of the simulated particles, calculated from the last 50 frames of the MD simulations at the GFNFF level of theory. Also shown are the average atomic weights of the different chemical compounds.

observed: 1.235 g cm^{-3}[39]) and the inorganic methyl-substituted compounds except $[(MeSi)_4S_6]$ (SI, Table S1).[39−42] The calculated results for $[(PhSi)_4S_6]$ $[(PhSn)_4S_6]$ and $[(NpSn)_4S_6]$ do not agree well with the corresponding crystalline structure but the order of magnitude is still comparable in these cases (determined: 1.566 g cm^{-3}, 2.218 g cm^{-3} and 2.072 g cm^{-3}, respectively; experimentally observed: 1.437 g cm^{-3},[1] 2.014 g cm^{-3}[42] and 1.79 g cm^{-3} [36], respectively). It should be mentioned that the experimentally measured density is the density of an amorphous powder.

The correlation between densities and atomic weights is almost perfect for the methyl-substituted molecules (Figure 5). For phenyl and naphthyl-substituted molecules the densities are slightly higher than the average atomic weights would suggest. This indicates a more dense packing of molecules with larger substituents in the solid, due to the larger binding energies. The increasing binding energy with increasing substituent size was already found and described by considering the interaction of dimer model systems.[16]

Statistical Analysis of Bond Parameters. Statistical examination of the bond lengths and angles reveals overall expected trends (Tables S2 and S3). The T−E bond lengths of the molecules with the composition $[(RT)_4E_6]$ (R = Me, Ph,

Np; T = C, Si, Ge, Sn; E = S, CH_2) increase as expected from $\{CH_4(CH_2)_6\}$ (1.56 Å) via $\{Si_4S_6\}$ (2.17 Å) and $\{Ge_4S_6\}$ (2.23 Å) to $\{Sn_4S_6\}$ (2.42 Å). The substituents have no significant effect on the T−E bond lengths. The standard deviation of the T−E bond lengths is quite small for all systems (<2.5%), which means that hardly any vibrations with significant bond length changes are excited at 300 K.

The T−E−T bond angles show larger standard deviations in the range of 2.5−7%. Larger changes of the bond angles especially occur for the inorganic core structures. Here the standard deviation of the T−E−T bond angles increases from the adamantane based structure through the Si and Ge based structures to the Sn based structures. This indicates the presence of deformation vibrations within the core structure at 300 K. Furthermore, the $\{Sn_4S_6\}$ core structure can be expected to be more flexible than the $\{Si_4S_6\}$ and $\{Ge_4S_6\}$ core structures. The organic adamantane units remain almost unaffected by these core deformation vibrations. The more flexible molecular structures can be associated with a lower order of the molecules in the solid, which is why $\{Sn_4S_6\}$ based structures tend to adopt an amorphous structure rather than, e.g., $\{Si_4S_6\}$ based structures. In fact, $[(PhSi)_4S_6]$ forms a crystalline structure while $[(PhSn)_4S_6]$ is amorphous.[16]

Analysis of Pair Distribution Functions (PDFs). In Figure 6, we show the total PDF of the four different core-

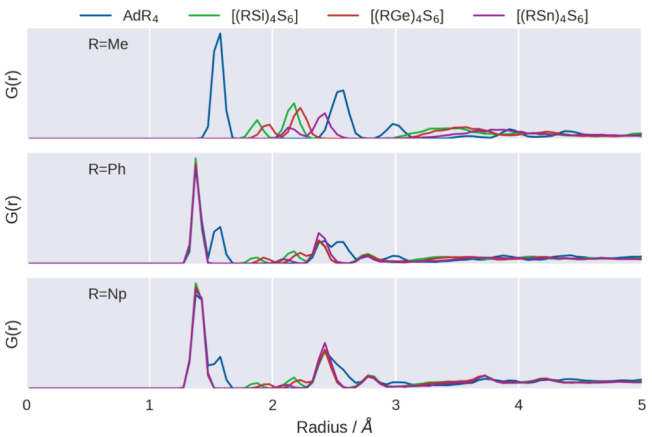

Figure 6. Total, normalized PDF of the different chemical compositions AdR_4 (R = Me, Ph, Np) and $[(RT)_4]S_6$ (R = Me, Ph, Np, and *T* = Si, Ge, Sn) with respect to all heavy atom types. The figure is divided into three sections: molecules with methyl substituents (top), phenyl substituents (middle) and naphthyl substituents (bottom). We limit the consideration of the total PDFs to 5 Å. This gives a good representation of the atomic structure within a molecule as well as the closest atoms of directly neighboring atoms. Individual PDFs are shown in Figure S8.

systems with the same substituent-type in one plot. For simplicity, we have excluded the hydrogen atoms from the total PDF, but a PDF with hydrogen atoms is given in Figure S6. The well-defined peaks below 3 Å represent the well-defined atomic structures within the molecules. The absence of such well-defined peaks beyond 3−4 Å in Figures 6 and S6 indicates an amorphous character of the simulated particles.

For $AdMe_4$, a large peak at 1.5−1.6 Å represents the C_{sp3}−C_{sp3} bonds within the adamantane cage. The second peak at about 2.5 Å is the second order bond of two sp^3 C atoms, the peak at 3 Å is the third order bond. For the inorganic structures with Me substituents there are two peaks at 1.8 Å and 2.5 Å depending on the elements in the cluster. These are first the T−C_{Sub} bonds and second the T−E bonds. All these peaks representing the core structure are also observed for the phenyl and naphthyl-substituted compounds. In addition to these core related peaks, the peaks at about 1.4 Å represent the first order C_{sp2}−C_{sp2} bonds of the phenyl and naphthyl substituents and at 2.8 Å, the second order C_{sp2}−C_{sp2} bonds are present. All these mentioned peaks are illustrated in Figure 7.

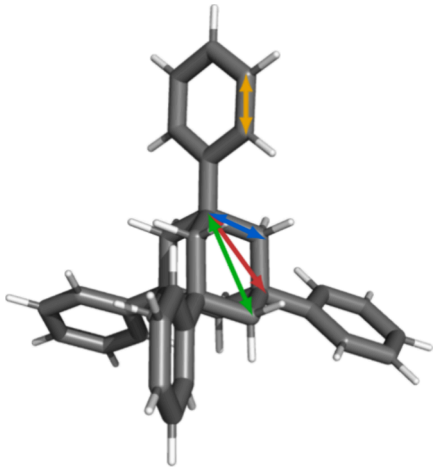

Figure 7. Sketch of the distances of the occurring PDF peaks in Figure 6. The blue arrow symbolizes the direct T−E bond (1.54 Å for $AdPh_4$), the red arrow symbolizes the second order contact (2.55 Å for $AdPh_4$), and the green arrow the third order contact (2.95 Å for $AdPh_4$). The orange arrow indicates the first-order bond within the aromatic substituents (1.39 Å for $AdPh_4$). The second and third order bond length of the aromatic substituents are 2.42 and 2.78 Å.

A better analysis of the amorphous nature of the systems can, however, be derived from PDFs. Thus, we analyzed PDFs within 20 Å considering the center of mass of the whole molecules (PDF_{mol}, Figure 8) and the center of mass of the substituents (PDF_{sub}, Figure 10). A sketch of the intermolecular distances is shown in 9.

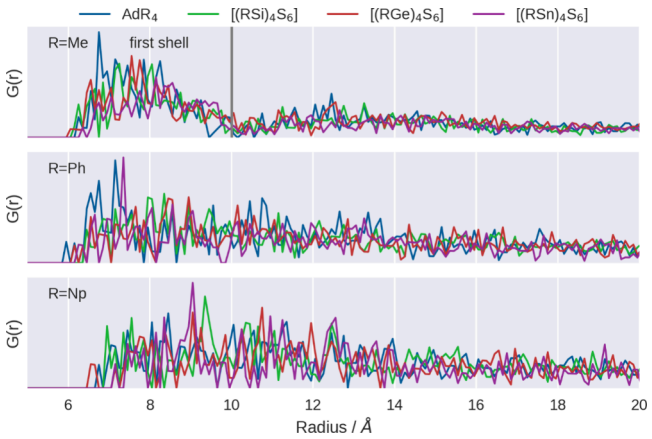

Figure 8. PDF_{mol} of the different chemical compositions (AdR_4 (R = Me, Ph, Np) and $[(RT)_4]S_6$ (R = Me, Ph, Np, and *T* = Si, Ge, Sn) with respect to the center of mass of the whole molecules. The figure is divided into three sections: molecules with methyl substituents (top), phenyl substituents (middle), and naphthyl substituents (bottom). Individual PDFs are shown in Figure S9.

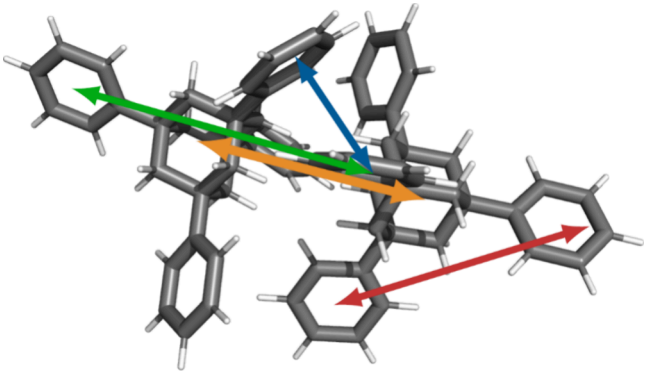

Figure 9. Sketch of the distances of the occurring PDF peaks in Figures 8 and 10. The orange arrow represents the distance of the center of mass of the $AdPh_4$ dimer (5.98 Å). The blue arrow represents the intermolecular substituent-substituent distance of close substituents (5 Å), the red arrow represents the intramolecular substituent-substituent distance (7.5 Å) and the green arrow represents the intermolecular substituent-substituent distance of distant substituents (10 Å).

The PDF_{mol} of the methyl-substituted compounds shows a clear but very broad peak in the range of 6 to 10 Å, which represents the first coordination shell around the molecules. The PDF_{mol} at 10 Å indicates the absence of molecules at this distance. Thus, there is a separation of the nearest neighbor shell from the more distant molecules in the PDF_{mol}. Further, a second neighborhood shell can be discernible for the methyl-substituted compounds.

For the PDF_{mol} of compounds with phenyl and naphthyl substituents, no such nearest neighbor shell is detected from the radial distance alone, as the distances of the centers of mass vary depending on the orientation of each molecule. The different dimer conformers have been discussed in our previous work.[16] For the compounds $AdPh_4$, $[(PhSn)_4S_6]$ and $[(NpSn)_4S_6]$, however, a first shell can also be discerned, see also individual PDFs in Figure S9 in the SI.

Finally, we discuss the PDF_{sub} that corresponds to the centers of mass of the substituents, see Figure 10. The

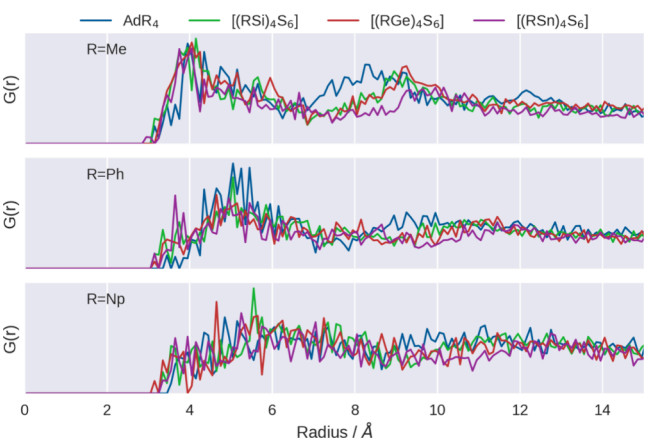

Figure 10. PDF_{sub} of the different chemical compositions AdR_4 (R = Me, Ph, Np) and $[(RT)_4]S_6$ (R = Me, Ph, Np, and T = Si, Ge, Sn) with respect to the center of mass of the substituents, excluding the substituents of the same molecule. The figure is divided into three sections: molecules with methyl substituents (top), phenyl substituents (middle), and naphthyl substituents (bottom). Individual PDFs are shown in Figure S10.

intramolecular interactions are excluded in Figure 10, as they are determined by the atomic structure of the cluster molecules and are therefore well defined. In contrast to the intramolecular distances, the intermolecular distances are less well defined.[16] In our previous work, we identified several different dimer conformers.[16]

For all structures, regardless of the core structure, we find a broad peak starting at about 3 Å and reaching up to 5−6 Å, which represents the intermolecular substituent-substituent interaction. For the methyl-substituted systems, a second neighbor-shell can be identified. The second neighbor-shell starts at about 6−7 Å and reaches toward 11−12 Å. However, this neighboring shell is already much less well-defined and shallower than the first shell. The second shell is also more well-defined, the smaller the substituent. For methyl-substituted systems, the second shell is quite well-defined, for phenyl and naphthyl-substituted systems it is much less well-defined.

In summary, the PDF_{mol} results show a broad first nearest neighbor coordination shell for the methyl-substituted structures and the PDF_{sub} indicates clear distances below 10 Å. Since the methyl-substituted adamantane molecules form ordered structures, as experimentally shown,[35−37] this could be interpreted as the beginning of order in the system.[1] For the phenyl and naphthyl-substituted compounds no or only a very faint first nearest neighbor coordination shell was found. The intermolecular distances for Ph and the intramolecular and intermolecular distances for Np overlap and vary, making an interpretation of the corresponding PDF_{sub} difficult.

Angle Dependent Neighborhood Analysis. The PDFs are limited to the radial distribution and therefore have the disadvantage of not considering the angular dependent close-range order of the materials. To account for the angular dependence of the relative orientation of the molecules, we analyzed the relative position of the molecules to each other, including their relative angles. To do this, we extracted dimer structures from the 50 frames of the trajectory. We fitted one of the molecules to a reference molecule, as described in the Methods section. From this fitted dimer, we calculated the azimuth and polar angles and the distance, as shown in Figure 3.

This angular dependent neighborhood analysis shows for the methyl-substituted structures (Figure 11, top) a very low density of neighboring molecules in the polar angle at $\theta = 0°$. The region around the polar angle of $\theta = 180°$ contains a few but very close neighboring molecules (Figures 11), which prevent the presence of other molecules within the given distance range. This is because the substituent of the reference molecule that coincides with this axis leads to steric hindrance of other molecules in this region. Other regions with a low density of neighboring molecules are the areas with azimuth angles $\varphi = 0°$, $\varphi = 120°$ and $\varphi = 240°$. The substituents of the other molecules are in these regions, which leads to steric hindrance.

For the phenyl substituents, the same low-density regions of neighboring molecules are present at $\varphi = 0°$, $\varphi = 120°$ and $\varphi = 240°$ and $\theta = 0°$ and $\theta = 180°$ (Figure 9, middle row). However, in contrast to the methyl-substituted compounds, the phenyl-substituted compounds have less-pronounced regions of low density. In all four core structures the high-density regions predominate in a similar pattern to the methyl-substituted compounds and become more defined with increasing core size. This trend is even more pronounced for

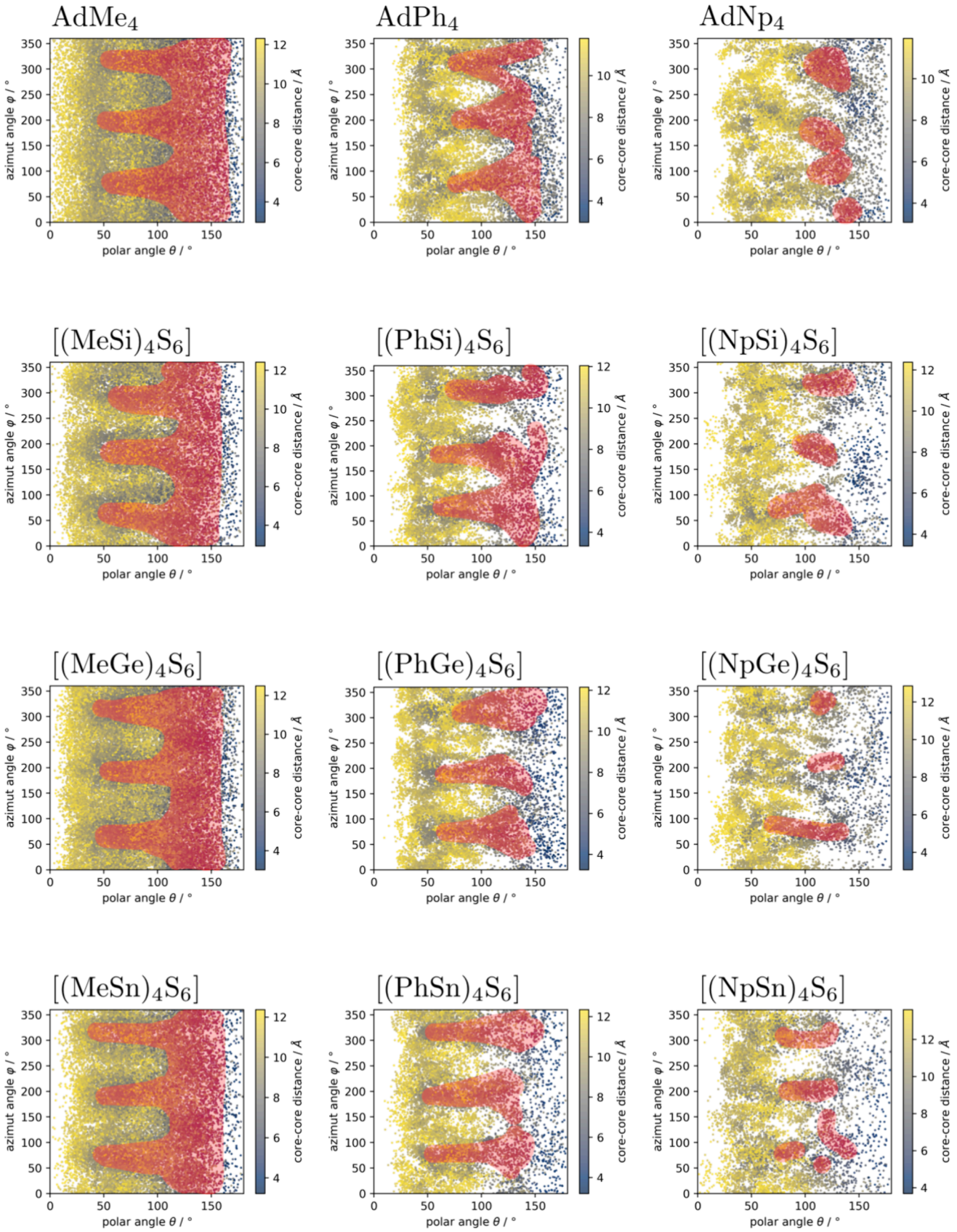

Figure 11. Angle-dependent neighboring analysis of the relative positions of molecules within extracted dimers with a core−core distance less than twice the core−core distance from the last 50 frames of the MD simulation (GFNFF level of theory). Shown are the positions of neighboring molecules around a reference molecule as a function of their polar angles, azimuth angles and core−core distances, as explained in Figure 3. Areas of high next-neighbor density are maked red.

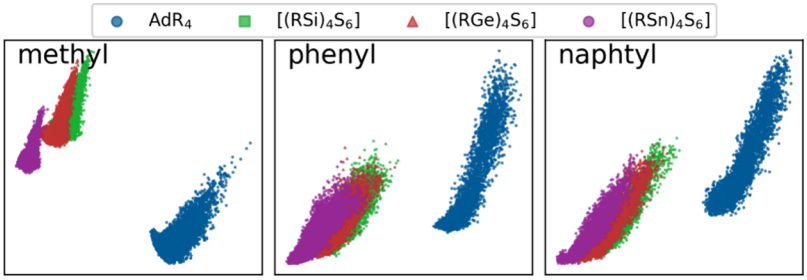

Figure 12. Dimensionally reduced power spectra of SOAP-analyzed, unified dimer structures for the last 50 structures of the MD simulations of (a) methyl-substituted structures, (b) phenyl-substituted structures and (c) naphthyl-substituted structures. The different core structures are color coded for distinction.

the naphthyl-substituted structures. In these cases the regions of low density around $\varphi = 0°$, $\varphi = 120°$, and $\varphi = 240°$ are barely discernible and the plots are dominated by local patches of high structure density.

Overall, the core structure has a much smaller influence on the distribution of the molecules than the substituent structure. Comparing $AdMe_4$, $[(MeSi)_4S_6]$, $[(MeGe)_4S_6]$, and $[(MeSn)_4S_6]$, the general trend remains the same throughout the different core structures. The same is true for the other systems with the same substituents. This behavior toward more local, small areas with high density of neighboring molecules from methyl to phenyl to naphthyl substituents can be explained by an increasing near order with increasing substituent size.

For example, compounds with naphthyl substituents have a more defined near order than compounds with phenyl substituents. This also leads to an increased order in the macroscopic structure and thus a greater tendency to crystalline habit in solids. This conclusion extends the findings of the PDFs. The inclusion of the angular dependence is necessary to describe the near order and indeed leads to conclusions in agreement with experimental studies, e. g., $[(NpSn)_4S_6]$ shows more order and crystallinity than $[(PhSn)_4S_6]$.[17] The much smaller methyl substituents show properties different from the phenyl and naphthyl-substituted structures due to their very small substituent-substituent interaction. The small substituents lead to increased order in the materials, as seen from the PDF and therefore favor the crystalline habitus.

Similarity Analysis. Finally, we compared the dimensionally reduced power spectrum obtained from a SOAP analysis of the extracted dimer structures, see Figure 12. Note that data points close to each other represent dimer structures that are like each other. We only compare compounds with the same substituents, as compounds with different substituents lead to fundamentally different power spectra and are therefore not comparable.

The SOAP-based plots clearly show a high similarity of the inorganic compounds for each type of substituent. In particular, $\{Si_4S_6\}$ and $\{Ge_4S_6\}$ overlap considerably. The slight shift of the inorganic structures from right to left in $\{Si_4S_6\}$, $\{Ge_4S_6\}$, and $\{Sn_4S_6\}$ is a consequence of the size of the core structures and the resulting stronger core−core interactions and a larger core-volume (core-volume from convex hull: $\{Si_4S_6\}$: 27 Å^3, $\{Ge_4S_6\}$: 30 Å^3, $\{Sn_4S_6\}$: 38 Å^3).[16] This shift is most pronounced for the methyl-substituted structures and less pronounced for the phenyl and naphthyl-substituted structures. For the phenyl and naphthyl-substituted structures, the substituent-substituent interaction becomes more dominant compared to the core−core interaction and therefore the structures are more similar overall, although the core structures are different. The adamantane structures differ significantly from the inorganic structures, which is to be expected given the small core volume (9 Å^3).

DISCUSSION AND CONCLUSION

Structural information on amorphous cluster materials is hardly accessible by computational modeling due to the size limitations imposed by the method used and the periodic boundary conditions for the calculation of solids. However, accurate models of amorphous cluster materials are needed to determine differences in their microscopic structures with respect to the near order. The particle approach at GNF-FF level of theory was used to model amorphous cluster materials and the analysis of these particles provides valuable insights into their geometric structures. It should be noted that with this particle approach amorphous structures with no far order are always generated and therefore the near order or beginning order in the materials can be investigated. This is used to interpret tendencies of the materials toward crystallinity as incipient order in the system.

The similarity analysis based on SOAP shows that the organic adamantane is clearly different from the inorganic compounds. This is due to the different adamantane core radii of the materials. The inorganic compounds themselves show only minor differences, with the compounds containing the $\{Sn_4S_6\}$ core being the most different from the inorganic compounds.

From the statistical analysis of the bonding parameters, we found an increasing flexibility of the molecular core structure with increasing core size (Ad < $\{Si_4S_6\}$ < $\{Ge_4S_6\}$ < $\{Sn_4S_6\}$). This is consistent with the experimentally observed tendency that $\{Sn_4S_6\}$-based macroscopic structures generally tend toward an amorphous habitus compared to, for example $\{Si_4S_6\}$-based macroscopic structures.

The PDF_{mol} indicate a first coordination shell for the methyl-substituted compounds, but no clear distinction of the coordination shells for the phenyl- and naphthyl-substituted compounds. These results for the methyl-substituted compounds can be interpreted with a beginning order in the materials and are consistent with the higher order of methyl-substituted clusters despite the large core−core interaction.[1] The overlap and variation of the intermolecular distances for Ph and the intramolecular and intermolecular distances for Np make the interpretation of the PDF_{sub} difficult.

The angle-dependent neighborhood analysis of extracted dimer structures indicates a lower structural variation for larger substituents (Me < Ph < Np), which can be associated with a

higher near order in the material. For compounds with phenyl and naphthyl substituents, this observation is consistent with experimental studies, where, for example, $[(NpSn)_4S_6]$ exhibits enhanced π-π stacking compared to $[(PhSn)_4S_6]$, which leads to increased long-range order for $[(NpSn)_4S_6]$.

Comparison with experimental data supports the findings and the used model system. This shows that the proposed particle-based model, at a sufficient system size, is suitable to describe amorphous materials.

Overall, further details from the geometric structures of the molecular tetrel chalcogenide cluster materials can be gleaned through the present investigation of the amorphously modeled materials. The initial order in the materials seems to arise from a combination of the flexibility of the core structures and the variation of the neighborhood interactions by the substituents. In contrast, for the methyl-substituted compounds, there appears to be incipient order through the formation of coordination shells.

AUTHOR INFORMATION

Corresponding Author

Doreen Mollenhauer − *Institute of Physical Chemistry, Justus Liebig University, Giessen 35392, Germany; Center for Materials Research, Justus Liebig University, Giessen 35392, Germany;* orcid.org/0000-0003-0084-4599; Email: Doreen.Mollenhauer@phys.chemie.uni-giessen.de

Authors

Sebastian Schwan − *Institute of Physical Chemistry, Justus Liebig University, Giessen 35392, Germany; Center for Materials Research, Justus Liebig University, Giessen 35392, Germany*

Benjamin D. Klee − *Department of Chemistry, Philipps University Marburg, Marburg 35043, Germany; Wigner Research Centre for Physics, Budapest 1121, Hungary*

Niklas Rinn − *Institute of Nanotechnology, Karlsruhe Institute of Technology, Karlsruhe 76131, Germany*

Peter R. Schreiner − *Center for Materials Research, Justus Liebig University, Giessen 35392, Germany; Institute of Organic Chemistry, Justus Liebig University, Giessen 35392, Germany;* orcid.org/0000-0002-3608-5515

Stefanie Dehnen − *Institute of Nanotechnology, Karlsruhe Institute of Technology, Karlsruhe 76131, Germany;* orcid.org/0000-0002-1325-9228

Wolf-Christian Pilgrim − *Department of Chemistry, Philipps University Marburg, Marburg 35043, Germany*

Complete contact information is available at: https://pubs.acs.org/10.1021/acs.jctc.4c00196

Author Contributions

The manuscript was written through contributions of all authors. All authors have given approval to the final version of the manuscript.

Funding

This work was supported by the German Research Foundation within the framework of FOR2824.

Notes

The authors declare no competing financial interest.

ACKNOWLEDGMENTS

This work was supported by the German Research Foundation within the framework of FOR2824 (project number: 398143140). The authors acknowledge computational resources provided by the HPC Core Facility and the HRZ of the Justus-Liebig-University Giessen. B.D.K. was supported by the ELKH (Eötvös Loránd Research Network) grant SA-89/2021 (Structure of energy storage materials).

REFERENCES

(1) Rosemann, N. W.; Eußner, J. P.; Dornsiepen, E.; Chatterjee, S.; Dehnen, S. *J. Am. Chem. Soc.* **2016**, *138*, 16224−16227.

(2) Rosemann, N. W.; Eußner, J. P.; Beyer, A.; Koch, S. W.; Volz, K.; Dehnen, S.; Chatterjee, S. *Science* **2016**, *352*, 1301−1304.

(3) Alfano, R. R. *The Supercontinuum Laser Source*; Springer New York: New York, NY, 2016.

(4) Birks, T. A.; Wadsworth, W. J.; Russell, P. St. J. *Opt. Lett.* **2000**, *25*, 1415−1417.

(5) Husakou, A. v.; Herrmann, J. *Phys. Rev. Lett.* **2001**, *87*, No. 203901.

(6) Paulsen, H. N.; Hilligse, K. M.; Thøgersen, J.; Keiding, S. R.; Larsen, J. J. Coherent anti-Stokes Raman scattering microscopy with a photonic crystal fiber based light source. *Opt. Lett.* **2003**, *28*, 1123−1125.

(7) Kano, H.; Hamaguchi, H. *Appl. Phys. Lett.* **2004**, *85*, 4298.

(8) Bourquin, S.; Aguirre, A. D.; Hartl, I.; Hsiung, P.; Ko, T. H.; Fujimoto, J. G.; Birks, T. A.; Wadsworth, W. J.; Bünting, U.; Kopf, D. *Opt. Express* **2003**, *11*, 3290−3297.

(9) Rosemann, N. W.; Locke, H.; Schreiner, P. R.; Chatterjee, S. White-Light Generation through Nonlinear Optical Response of 1, 3, 5, 7-Tetraphenyladamantane: Amorphous versus Crystalline States. *Adv. Opt. Mater.* **2018**, *6*, 1701162.

(10) Berndt, J.-P.; Engel, A.; Hrdina, R.; Dehnen, S.; Schreiner, P. R. *Organometallics* **2019**, *38*, 329−335.

(11) Hanau, K.; Schwan, S.; Schäfer, M. R.; Müller, M. J.; Dues, C.; Rinn, N.; Sanna, S.; Chatterjee, S.; Mollenhauer, D.; Dehnen, S. *Angew. Chem., Int. Ed.* **2021**, *60*, 1176−1186.

(12) Hanau, K.; Rinn, N.; Dehnen, S. *Inorg. Chem.* **2020**, *59*, 198−202.

(13) Hanau, K.; Rinn, N.; Argentari, M.; Dehnen, S. *Eur. J. Chem.* **2018**, *24*, 11711−11716.

(14) Dornsiepen, E.; Dobener, F.; Mengel, N.; Lenchuk, O.; Dues, C.; Sanna, S.; Mollenhauer, D.; Chatterjee, S.; Dehnen, S. *Adv. Opt. Mater.* **2019**, *7*, 1801793.

(15) Lunt, A. J. G.; Chater, P.; Korsunsky, A. M. On the origins of strain inhomogeneity in amorphous materials. *Sci. Rep.* **2018**, *8*, 1574.

(16) Schwan, S.; Achazi, A. J.; Ziese, F.; Schreiner, P. R.; Volz, K.; Dehnen, S.; Sanna, S.; Mollenhauer, D. *J. Comput. Chem.* **2023**, *44*, 843−856.

(17) Haust, J.; Belz, J.; Müller, M.; Danilo Klee, B.; Link Vasco, J.; Hüppe, F.; Rojas Lóon, I.; Christmann, J.; Beyer, A.; Dehnen, S.; Rosemann, N. W.; Pilgrim, W.; Chatterjee, S.; Volz, K. White Light Generating Molecular Materials: Correlation Between the Amorphous/Crystalline Structure and Nonlinear Optical Properties. *ChemPhotoChem* **2022**, *6*, No. e20220007.

(18) Spicher, S.; Grimme, S. *Angew. Chem., Int. Ed.* **2020**, *59*, 15665−15673.
(19) Grimme, S. *J. Chem. Theory Comput.* **2019**, *15*, 2847−2862.
(20) Pracht, P.; Bohle, F.; Grimme, S. *Phys. Chem. Chem. Phys.* **2020**, *22*, 7169−7192.
(21) Grimme, S.; Bannwarth, C.; Shushkov, P. *J. Chem. Theory Comput.* **2017**, *13*, 1989−2009.
(22) Pracht, P.; Caldeweyher, E.; Ehlert, S.; Grimme, S. A robust non-self-consistent tight-binding quantum chemistry method for large molecules. *ChemRxiv* **2019**, 1.
(23) Bannwarth, C.; Ehlert, S.; Grimme, S. *J. Chem. Theory Comput.* **2019**, *15*, 1652−1671.
(24) Martínez, L.; Andrade, R.; Birgin, E. G.; Martínez, J. M. *J. Comput. Chem.* **2009**, *30*, 2157−2164.
(25) Dornsiepen, E.; Dobener, F.; Chatterjee, S.; Dehnen, S. *Angew. Chem., Int. Ed.* **2019**, *58*, 17041−17046.
(26) Rojas-León, I.; Christmann, J.; Schwan, S.; Ziese, F.; Sanna, S.; Mollenhauer, D.; Rosemann, N. W.; Dehnen, S. Cluster-Glass for Low-Cost White-Light Emission. *Adv. Mater.* **2022**, 2203351.
(27) Virtanen, P.; Gommers, R.; Oliphant, T. E.; Haberland, M.; Reddy, T.; Cournapeau, D.; Burovski, E.; Peterson, P.; Weckesser, W.; Bright, J.; van der Walt, S. J.; Brett, M.; Wilson, J.; Millman, K. J.; Mayorov, N.; Nelson, A. R. J.; Jones, E.; Kern, R.; Larson, E.; Carey, C. J.; Polat, İ.; Feng, Y.; Moore, E. W.; VanderPlas, J.; Laxalde, D.; Perktold, J.; Cimrman, R.; Henriksen, I.; Quintero, E. A.; Harris, C. R.; Archibald, A. M.; Ribeiro, A. H.; Pedregosa, F.; van Mulbregt, P. SciPy 1.0: fundamental algorithms for scientific computing in Python. *Nat. Methods* **2020**, *17*, 261−272.
(28) Gereben, O.; Jóvári, P.; Temleitner, L.; Pusztai, L. A new Version of the RMC++ Reverse Monte Carlo Programme, Aimed at Investigating the Structure of Covalent Glasses. *J. Optoelectron. Adv. Mater.* **2007**, *9*, 3021−3027.
(29) Bartók, A. P.; Kondor, R.; Csányi, G. *Phys. Rev. B* **2013**, *87*, No. 184115.
(30) De, S.; Bartók, A. P.; Csányi, G.; Ceriotti, M. *Phys. Chem. Chem. Phys.* **2016**, *18*, 13754−13769.
(31) Jäger, M. O. J.; Morooka, E. V.; Federici Canova, F.; Himanen, L.; Foster, A. S. *NPJ Comput. Mater.* **2018**, *4*, 37.
(32) Himanen, L.; Jäger, M. O. J.; Morooka, E. V.; Federici Canova, F.; Ranawat, Y. S.; Gao, D. Z.; Rinke, P.; Foster, A. S. *Comput. Phys. Commun.* **2020**, *247*, No. 106949.
(33) Yang, J.; De, S.; Campbell, J. E.; Li, S.; Ceriotti, M.; Day, G. M. *Chem. Mater.* **2018**, *30*, 4361−4371.
(34) Engel, E. A.; Anelli, A.; Ceriotti, M.; Pickard, C. J.; Needs, R. J. *Nat. Commun.* **2018**, *9*, 2173.
(35) Musil, F.; De, S.; Yang, J.; Campbell, J. E.; Day, G. M.; Ceriotti, M. *Chem. Sci.* **2018**, *9*, 1289−1300.
(36) Link Vasco, J.; Stellhorn, J. R.; Klee, B. D.; Paulus, B.; Belz, J.; Haust, J.; Hosokawa, S.; Hayakawa, S.; Volz, K.; Rojas León, I.; Christmann, J.; Dehnen, S.; Pilgrim, W. C. *J. Phys.: Condens. Mat.* **2023**, *35*, 384001.
(37) Klee, B. D.; Paulus, B.; Link Vasco, J.; Hosokawa, S.; Stellhorn, J. R.; Hayakawa, S.; Dehnen, S.; Pilgrim, W.-C. *Scr. Mater.* **2022**, *219*, No. 114851.
(38) Stellhorn, J. R.; Hayakawa, S.; Klee, B. D.; Paulus, B.; Link Vasco, J.; Rinn, N.; Rojas León, I.; Hosier, C. A.; Dehnen, S.; Pilgrim, W. *Adv. Opt. Mater.* **2023**, *11*, 2201932.
(39) Bart, J. C. J.; Daly, J. J. *J. Chem. Soc., Dalton Trans.* **1975**, *20*, 2063−2068.
(40) Benno, R. H.; Fritchie, C. J. *J. Chem. Soc., Dalton Trans.* **1973**, *5*, 543−546.
(41) Kobelt, D.; Paulus, E. F.; Scherer, H. *Acta Crystallogr.* **1972**, *B28*, 2323−2326.
(42) Klee, B. D.; Dornsiepen, E.; Stellhorn, J. R.; Paulus, B.; Hosokawa, S.; Dehnen, S.; Pilgrim, W. *Phys. Status. Solidi B* **2018**, *255*, 1800083.